

www.acsanm.org Article

Multivariate Analysis on the Structure—Activity Parameters for Nano-CuO_x-Catalyzed Reduction Reactions

Lorianne R. Shultz-Johnson, Matthew Chang, Neil N. Bisram, Jacob T. Bryant, Christopher P. Martin, Azina Rahmani, Jacob I. Furst, Jonathan D. Caranto, Parag Banerjee,* Fernando J. Uribe-Romo,* Daniel R. Gamelin,* and Titel Jurca*



Cite This: ACS Appl. Nano Mater. 2024, 7, 928–939



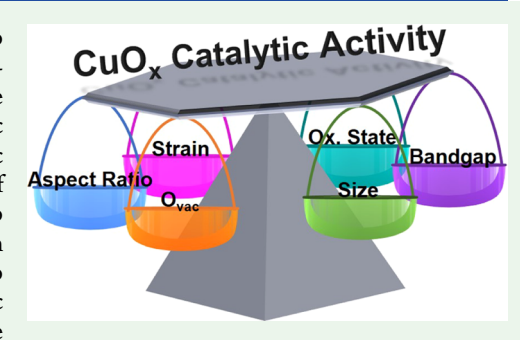
ACCESS

Metrics & More



SI Supporting Information

ABSTRACT: Understanding the origin of enhanced catalytic activity is critical to heterogeneous catalyst design. This is especially important for non-noble metal-based catalysts, notably metal oxides, which have recently emerged as viable candidates for numerous thermal catalytic processes. For thermal catalytic reduction/hydrogenation using metal oxide nanoparticles, enhanced catalytic performance is typically attributed to an increased surface area and the presence of oxygen vacancies. Concomitantly, the treatments that induce oxygen vacancies also impact other material properties, such as the microstrain, crystallinity, oxidation state, and particle shape. Herein, multivariate statistical analysis is used to disentangle the impact of material properties of CuO nanoparticles on catalytic rates for nitroaromatic and methylene blue reduction. The impact of the



microstrain, shape, and Cu(0) atomic percent is demonstrated for these reactions; furthermore, a protocol for correlating material property parameters to catalytic efficiency is presented, and the importance of catalyst design for these broadly utilized probe reactions is highlighted.

KEYWORDS: catalytic defects, heterogeneous catalysis, nanocatalysis, 4-nitrophenol reduction, methylene blue reduction, structure—activity relationship, multivariate analysis

INTRODUCTION

The development of efficient, sustainable, and selective nanocatalysts for nitro- and heterocyclic reductions spans importance across agricultural, environmental, pharmaceutical, and industrial applications. 1-3 Many noble metal-based nanocatalysts demonstrate high activity for these reactions yet their scarcity and associated cost prevents broader-scale application.4 More recently, earth-abundant transition metal oxide-based catalysts have shown competitive reactivity. 5,6 Although numerous variations of earth-abundant transition metal catalysts have been tested, the nature of their active sites often remains enigmatic, leading to a more Edisonian approach to catalyst design. Among these, copper oxides have garnered particular interest due to their high conductivity, which increases electron transfer and reactivity for photocatalytic C–C coupling, benzyl alcohol oxidation, s,9 carbon dioxide reduction, and nitro group reductions. Much like other metal oxides, the origin of their activity remains ambiguous. For example, Pal et al. used Cu₂O catalysts to reduce 4nitrophenol (4NP) in the presence of NaBH₄ and found that in situ Cu(0) and Cu(II) were produced; Cu(0) from reduction with NaBH₄ and Cu(II) from either oxidation with dissolved oxygen or due to the alkaline solution (pH \sim 9). They posited that the in situ Cu(0) facilitated the hydride transfer from BH₄⁻ as well as the adsorption of 4NP.

Conversely, other studies have found that Cu₂O has higher catalytic activity than metallic copper,¹⁴ although both species have poor stability. Still, many other reports attribute increased reactivity for these reactions to increased surface area and oxygen vacancies.^{15–17} Li et al. recently elucidated experimentally and computationally that oxygen vacancies in copper oxide-based catalysts supported on cerium oxide change the electron density and polarity; this resulted in more ionic Cu–O bond character, which increased reactivity for hydroboration reactions.¹⁸ Likewise, one of our groups has recently reported on the enhanced reactivity in copper oxide-based nanocatalysts for nitrophenol reduction with increased oxygen vacancies.¹⁹

Oxygen vacancies in metal oxides will provide partially reduced neighboring metals, which can increase conductivity and charge transfer. These vacancies may change the crystal structure and induce more reactive binding sites and bond activation for the substrate of interest. Many reports

Received: October 18, 2023 Revised: December 7, 2023 Accepted: December 12, 2023 Published: January 2, 2024





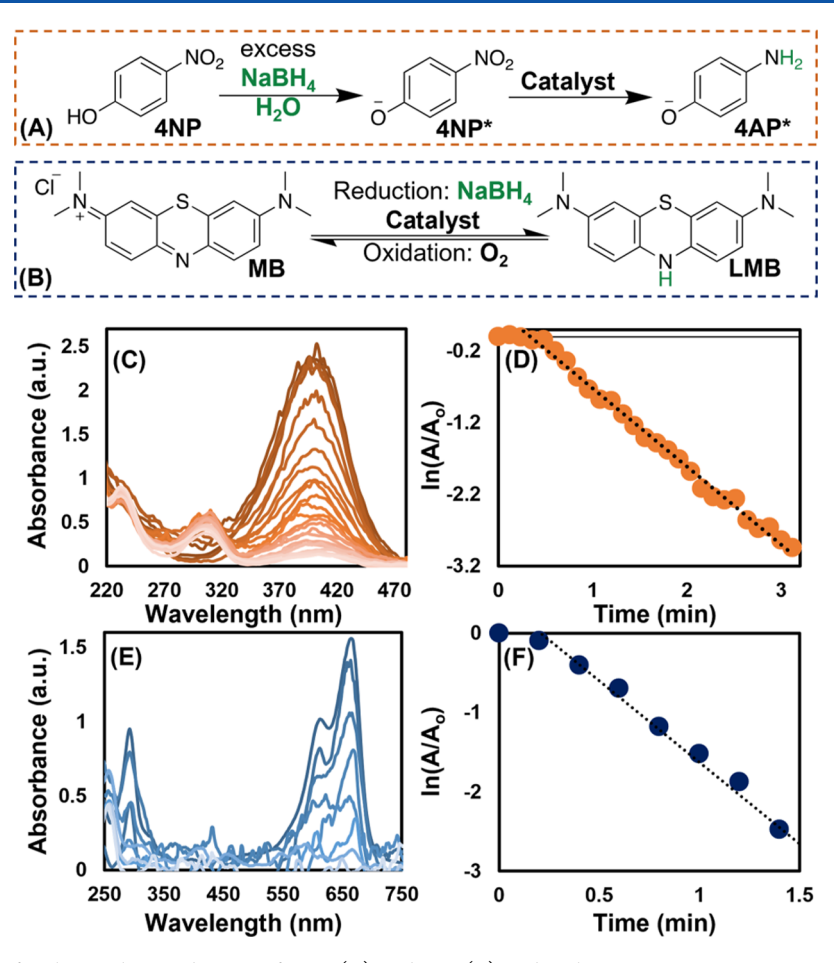


Figure 1. Reaction schemes for the catalytic reduction of 4NP (A) and MB (B) and with representative UV-vis spectra and pseudo-first-order kinetics for the reduction of 4NP (C, D) and MB (E, F).

have correlated a general increase in the prevalence of oxygen vacancies to an increase in catalytic activity for redox reactions. ^{15,17} However, treatments used to induce oxygen vacancies on metal oxide nanoparticles not only produce these vacancies but may also alter the crystalline structure and particle morphology, change crystalline microstrain, induce other atom defects, fully reduce metal sites, and change the concentration of terminal groups. Yet, conventionally, any increase in catalytic activity is typically only attributed to oxygen vacancies without evaluating the impact of these other changes to the material properties. This begs the question: are oxygen vacancies the most important material property when it comes to catalytic reactivity, or could there be collateral changes that also have a measurable impact?

To systematically study the structure—reactivity relationships of CuO, we first produced control CuO nanoparticles, which we then subjected to several forms of postprocessing to induce defects, modulate the oxidation state, and modify the particle size. All of the resulting particles were extensively characterized to elucidate material differences, and their catalytic activity toward the reduction of 4NP and methylene blue (MB) was tested. The resulting materials' characterization and catalytic results were correlated through multivariate analysis to disentangle the material's property—catalytic performance relationships. The two chosen catalytic reactions, reduction of 4NP and MB with NaBH₄ as the H-source (Figure 1A,B), are ubiquitous probe systems for heterogeneous catalyst validation that have been broadly studied in the

literature. 1,3 The broad utility of these reaction systems is predicated upon their facile monitoring through ultraviolet—visible (UV—vis) spectroscopy and their fit to simple kinetic models (e.g., concentration-dependent pseudo-first-order rate laws for 4NP reduction in the presence of excess NaBH₄, Figure 1C–F). 23

■ MATERIALS AND METHODS

Synthesis. Parent CuO particles were prepared through a hydrothermal process; 65 mL of 2.0 M NaOH solution was added dropwise into 100 mL of 0.2 M CuCl₂·(H₂O)₂ solution at 100 °C under continuous stirring, followed by cooling to room temperature and washing the resulting particles with copious amounts of deionized water. The particles were then separated into six batches and subjected to different post-treatments. Four of these batches were first calcined under air at 400 °C. Among these, one was left as is to be the control, labeled CuO_x-Cont. The other three were exposed to NaBH₄ treatment under sonication with varying concentrations and times to induce oxygen vacancies and partially reduce the oxidation state of copper.^{24,25} These materials are labeled as CuO_x-0.025M/15m, CuO_x-0.05M/5m, and CuO_x-0.05M/15m, named after their respective NaBH₄ treatment concentration (molarity) and time (minutes). The remaining two batches were first ball-milled for 2 h using a vibratory ball mill—an established method to induce oxygen vacancies without reducing the metal. 22,26 They were then calcined at 400 °C, one under air, which is expected to heal oxygen vacancies (labeled CuO_x-BM Cal. Air),²⁷ and the other under a nitrogen atmosphere to preserve oxygen vacancies (labeled CuOx-BM Cal. N_2). Following the preparation, the six different materials were

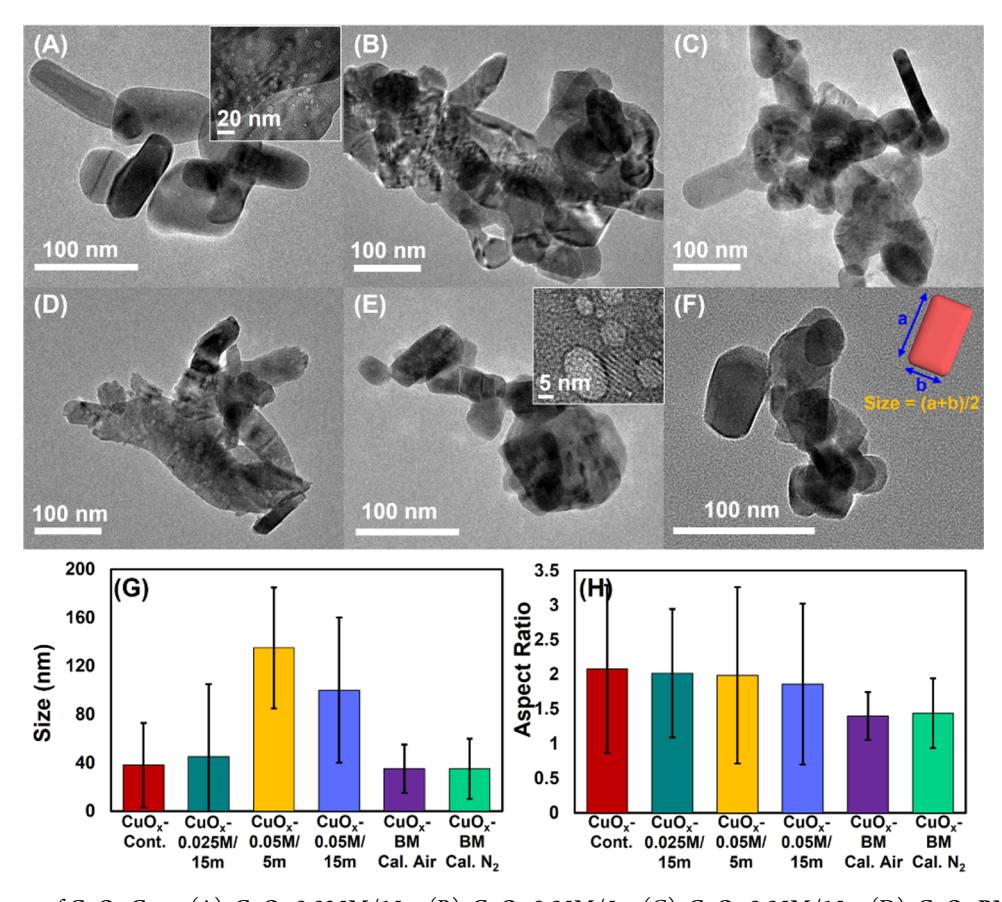


Figure 2. TEM images of CuO_x -Cont. (A), CuO_x -0.025M/15m (B), CuO_x -0.05M/5m (C), CuO_x -0.05M/15m (D), CuO_x -BM Cal. Air (E), and CuO_x -BM Cal. N_2 (F), as well as high-resolution TEM (A, E inset). Associated size distributions (G) are calculated by averaging the edge lengths [size = (a + b)/2] demonstrated in the inset (F) and aspect ratios [aspect ratio = a/b] (H).

extensively characterized to elucidate the impact of these post-treatments on the materials.

Characterization. Transmission electron microscopy (TEM) images of the six CuO_x samples were acquired using an FEI Tecnai G2 F20 supertwin microscope operating at 200 kV. Size distributions were obtained by measuring and taking the lengths of both the long and short edges of 35-100 particles per sample and obtaining the average of the Gaussian distribution produced. Powder X-ray diffraction (PXRD) data was obtained using a PANalytical Empyrean X-ray diffractometer in the Bragg-Brentano geometry with a 240 mm goniometer radius, with a 1.8 kW Ni-filtered Cu K α X-ray tube (λ = 1.540598 Å), 0.02 rad incident slit and 0.02° receiving Soller slit, a 0.125° divergent slit, a 0.5° antiscattering slit, a fixed 4 mm mask, and a Ni–Cu K β filter. X-ray photoelectron spectroscopy (XPS) analyses were conducted with an ESCALAB-250Xi+ spectrometer attached to an Al K α monochromatic X-ray source (20 mA, 15 kV). Thermogravimetric analysis (TGA) of all materials was conducted on an ISI TGA-1000 instrument housed inside a nitrogen atmosphere glovebox, using Pt sample pans and a 5 cm³ min⁻¹ flow of UHP N₂. Fourier transform infrared spectroscopy (FTIR) spectra were obtained on a Jasco 6600 with an attenuated total reflectance (ATR) attachment. Gas adsorption analysis was performed using a Micromeritics ASAP 2020 surface area and porosity analyzer at 77 K (liquid N_2 bath) for $N_2(g)$ on thermally activated samples. Electron paramagnetic resonance (EPR) spectra of powder samples were collected on a Magnettech ESR5000 spectrometer (Freiberg Instruments). Sample measurement was performed at 20 °C (293 K), which is consistent with similar measurements of CuO particles in the literature. 29,30 Notably, attempted measurements at 77 K did not improve the spectral resolution. Additional collection parameters for spectra are found in the Supporting Information. Absorption and diffuse reflectance measurements were performed with a Shimadzu UV-3600i Plus UV-vis-near-infrared (UV-vis-NIR) spectrophotometer by using an internal diffuse reflectance accessory for solidstate sample measurements. Further synthesis, characterization details, and collection parameters are given in the Supporting Information.

Catalytic Testing. The reduction of 4NP was monitored by UV–vis spectroscopy on an Agilent Cary 60 spectrophotometer. In a quartz cuvette, a 3 mL solution of 1.31 mM 4NP and 66.0 mM NaBH $_4$ was made. After an initial absorbance scan at t_0 , 1 mg of catalyst was added, and the reaction was monitored at timed intervals. The amount of catalyst is kept low to ensure sufficient points can be measured due to the high reaction rates. MB reduction reactions were performed in a similar manner with a 3 mL solution of 0.0278 mM MB and 43 mM NaBH $_4$.

■ RESULTS AND DISCUSSION

Characterization and Interpretation. Transmission electron microscopy (TEM) images of the particles were obtained, and size distributions were calculated by averaging the length of the long and short edges of the particles (Figure 2F, inset). The TEM images of CuO_x-Cont. revealed oblong particles with a Gaussian size distribution of 38 nm (Figure 2A,G). The large dispersity, represented by the error bars in Figure 2G, is not surprising considering that the size distributions were obtained by averaging the longest and shortest dimension and the fact that no surfactants for size control were utilized in the synthesis procedure. Specifically, surfactants were avoided as they may passivate surface active sites.³¹ With NaBH₄ post-treatment, the particles became slightly agglomerated (Figure 2B-D,G). Meanwhile, the ballmilled samples remained similar in size to CuO_x-Cont (Figure 2E-G). Typically, treatment with ball-milling can decrease the

particle size. In our case, overall particle size was not impacted; however, the shape was impacted as the oblong particles from the control were replaced with significantly lower aspect ratio particles. To better quantify this change, the average aspect ratios for all of the particles were measured. The aspect ratio for the $\text{CuO}_x\text{-Cont.}$ and NaBH_4 treated samples are similar, averaging \sim 2. The ball-milled samples, however, have decreased aspect ratios at \sim 1.4, indicating a more spherical shape. Nominally, this decreased aspect ratio may be attractive for catalytic activity as increased edge and corner sites have been associated with enhanced reactivity. $^{32-34}$

High-resolution (HR) TEM images of the CuO_x-Cont. and CuO_x-BM Cal. Air samples showed the presence of circular features on some of the particles (Figure 2A,E insets). The synthesis of the CuO particles under strong reducing conditions appears to cause the hollowing of the particles. We hypothesize this is due to the features being the same shade as the TEM grid and the precedence for CuO particle hollowing under comparatively mild conditions. 35,36 These images also suggest grain boundaries or smaller particles embedded into larger particles. Selected area electron diffraction (SAED) revealed that the CuO_x-Cont. particles were a mixture of single crystalline and polycrystalline phases, as indicated by the distinct spots and rings, respectively (Figures S2-S7). This corresponds well with the oblongshaped particles, the presence of different morphologies of the particles, and their size dispersity.

Gas adsorption measurements determined that the Brunauer–Emmett–Teller (BET) surface area differences between samples were negligible, with values ranging from $S_{\rm BET}=11.0$ to 12.4 m² g⁻¹ (Table S1). As there is no significant difference between samples, this parameter, which typically can be an important factor in differentiating catalyst performance, can be ignored, thus allowing a more focused comparison of other measured material properties. The TGA of the materials also showed very similar thermal stability and similar trends as those reported in the literature for CuO (Figure S9). The mass loss in the 230–330 °C region is attributed to non-CuO_x compounds such as residual NaOH or adsorbed organics and a decrease at >700 °C is attributed to the decomposition of the CuO particles.

Powder X-ray diffraction (PXRD) patterns of each sample were obtained (Figure 3A). The samples treated with 0.05 M NaBH₄ under sonication were plotted against three phases: CuO Cc space group (ICSD card 1646957),³⁹ Cu₂O Pn3m space group (ICSD card 1690293),40 and finally metallic copper in the Fm3m space group (ICSD card 1617943),⁴¹ showing good alignment. Thus, with more NaBH4 treatment, the copper oxide begins to reduce and becomes a mixed phase. While the CuO_x-0.025M/15m sample was treated with NaBH₄, it did not appear to be a mixed phase. To confirm this, a Rietveld refinement was performed on the pattern using GSAS-II software. 42 The pattern was best fit to only one phase of CuO in the C1c1 space group, confirming that no reduced copper oxide phases are observed in this sample (Figure S10). The PXRD patterns for CuO_x-Cont., CuO_x-BM Cal. Air, and CuO_r-BM Cal. N₂ samples also all appeared to be only the CuO monoclinic phase. Subtracting out the CuO_x-Cont. pattern from the ball-milled samples, however, revealed significant peak broadening for the treated samples, despite having similar particle size distributions (Figure S11). This indicates a possible increase in crystalline strain in the ballmilled samples. 43,44 To confirm this, the patterns were refined

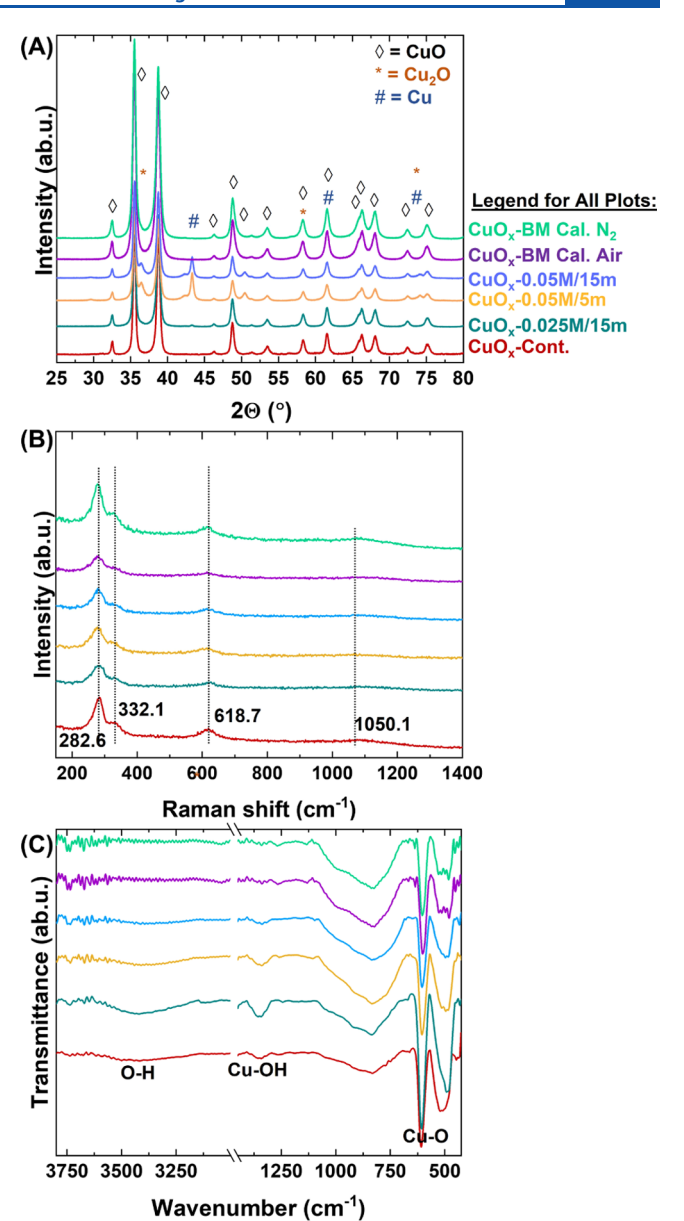


Figure 3. PXRD patterns of each of the materials (A), showing peaks for CuO in all samples and additional peaks characteristic of Cu_2O and Cu(0) in the 0.05 M NaBH_4 treated samples. Additional Raman (B) and FTIR (C) spectra of each material.

to obtain calculated microstrain values (Figure S10). Compared to the control with a microstrain of 1282.7 ppm $\Delta d/d$ units, the CuO_x-BM Cal. Air and CuO_x-BM Cal. samples had a ~5.5× and ~8.8× increase of microstrain, respectively, at 7112.4 and 11272.3 ppm $\Delta d/d$ units.

Raman spectra of all six samples show three well-defined peaks (Figure 3B). The CuO_x -Cont. sample reveals characteristic Raman bands at 282.6, 332.1, and 618.7 cm⁻¹ that are close to the wavenumbers identified as the first-order phonon scattering. The three peaks are assigned to the $\mathrm{A_g}$ and two $\mathrm{B_g}$ modes, originating from $\mathrm{Cu-O}$ vibrations. The peak at 282.6 cm⁻¹ is assigned to the $\mathrm{A_g}$, and the peaks at 332.1 and 618.7 cm⁻¹ are assigned to the $\mathrm{B_g}$ modes. The results indicate the presence of $\mathrm{Cu(II)}$ in the form of CuO in all six samples, in agreement with the PXRD data. The three highintensity Raman peaks of the CuO_x -0.05M/15m, CuO_x -0.05M/5m, and CuO_x -0.05M/15m samples shift slightly to

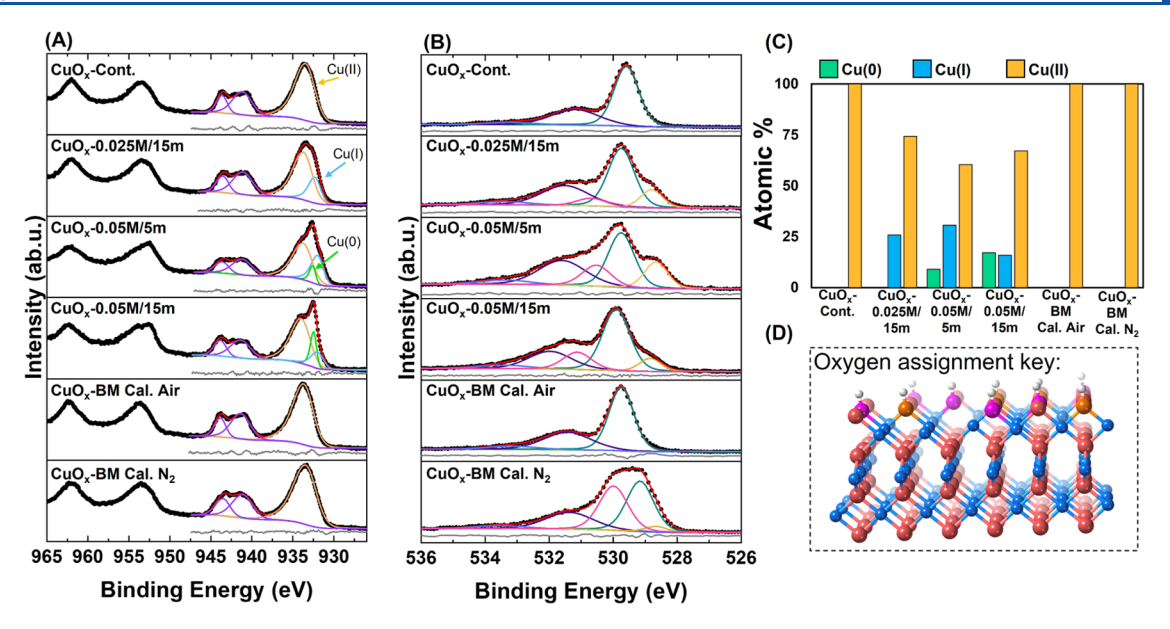


Figure 4. Stacked XPS spectra of all materials in the Cu 2p region (A) and the O 1s region (B) and calculated atomic percentages of each copper oxidation state from peak fitting (C). A schematic representation of oxygen peak assignments (D).

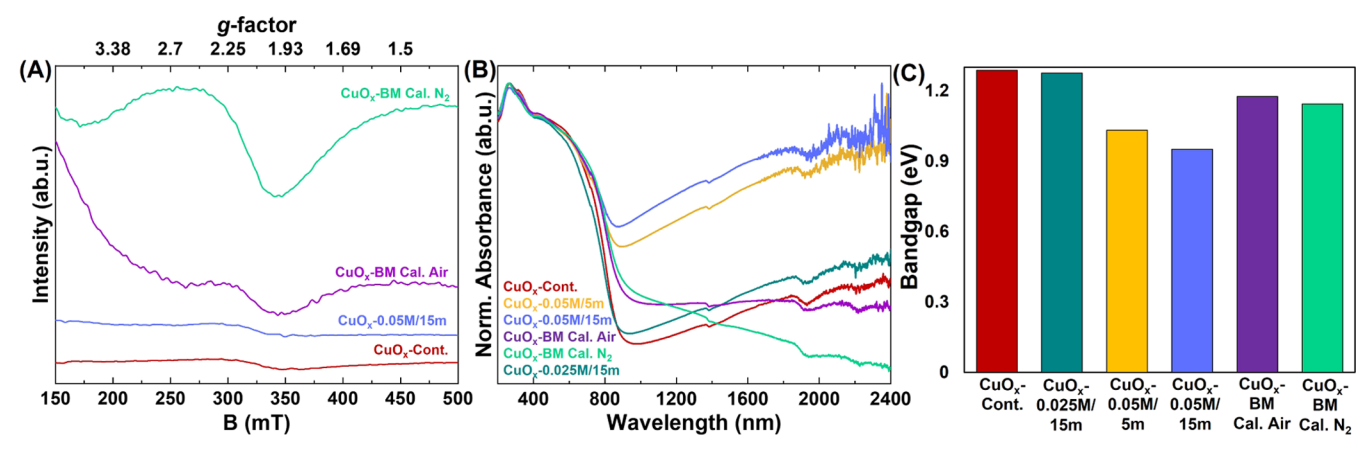


Figure 5. EPR overlaid spectra of the control, 0.05M/15m, and ball-milled samples (A), SS-UV-vis-NIR spectra of all samples (B), and calculated optical band gaps (C).

higher wavenumbers compared to the control. CuO_x-0.05M/5m shows the highest upshift since it has the largest particle size among these three samples. Xin et al. have previously reported that Raman peaks become stronger and shift to higher wavenumbers as grain size increases for CuO particles.⁴⁷ Furthermore, the Raman peaks of CuO_x-BM Cal. Air and CuO_x-BM Cal. N₂ samples shift to lower wavenumbers since they have slightly smaller particle sizes compared to the control sample. The peak at 1050.1 cm⁻¹ has previously been attributed to superoxide species, which may indicate the presence of oxygen vacancies on the surface of those samples.⁴⁸

The materials were further subjected to Fourier transform infrared (FTIR) spectroscopy measurements using attenuated total reflectance (ATR) (Figure 3C). The peaks centered around 490 and 605 cm⁻¹ are attributed to the A_u and B_u modes of CuO, stretching vibrations.⁴⁹ Meanwhile, the broad peak that spans $\sim\!690-1100$ cm⁻¹ is a poorly resolved combination of multiple signals. Peaks of interest in this region are at $\sim\!880$ cm⁻¹ attributed to Cu–OH and $\sim\!1060$ cm⁻¹ attributed to OH bending vibrations.^{50,51} This interpretation is supported by the presence of a peak around 1350 cm⁻¹ for some of the samples, which is assigned to Cu–

OH, and the broad peak around 3400 cm⁻¹ characteristic of O–H stretching vibrations.⁵⁰ It is noteworthy that the ball-milled samples do not have the characteristic Cu–OH peak around 1350 cm⁻¹, indicating that the ball-milling environment may decrease the concentration of the terminal hydroxyls.

X-ray photoelectron spectroscopy (XPS) was conducted on all of the materials to confirm the copper oxidation state and evaluate the presence of oxygen vacancies (Figure 4). The high-resolution (HR) Cu 2p spectrum for the CuO_x-Cont. sample is fitted to only one peak in the 2p_{3/2} region at 933.5 eV, commensurate with Cu(II) arising from CuO. 11,52,53 Likewise, the ball-milled samples show only the presence of Cu(II) for CuO. The CuO_x-0.025M/15m Cu 2p_{3/2} HRspectrum, however, is best fitted to two peaks: one characteristic of Cu(II) and a new peak corresponding to Cu(I) at 932.3 eV. 11,52,54 As the PXRD of this sample was best fit to only the CuO monoclinic phase, these reduced Cu(I) ions reside within the CuO monoclinic phase. With increased duration and/or concentration of NaBH₄ treatment for the CuO_x-0.05M/5m and CuO_x-0.05M/15m samples, the peak for Cu(I) increases, and a new peak characteristic of Cu(0) begins to appear at \sim 932.5 eV. 52,54,55 This is due to NaBH₄ starting to fully reduce

the copper metal on the surface of the particles, leading to a ternary-mixed phase (Figure 4A,C).

The CuO_x-Cont. HR O 1s spectrum features three peaks at 529.6, 531.2, and 533.2 eV attributed to lattice oxygen, ^{52,56} adsorbed hydroxyls, 57,58 and molecularly adsorbed oxygencontaining molecules such as water, respectively 57,59,60 (the synthesis and storage of the particles was under ambient conditions with ~55% relative humidity). Interestingly, the CuO_x-BM Cal. Air particles had an almost identical O 1s spectrum, indicating that any oxygen vacancies that may have formed during ball-milling were healed under calcination in air. The NaBH₄-treated samples feature two additional peaks: one at a binding energy higher than that of the lattice oxygen peak $(530.8 \pm 0.2 \text{ eV})$ and one at a lower binding energy $(528.77 \pm$ 0.1 eV). The higher binding energy peak is attributed to hydroxyl groups adsorbed into lattice oxygen vacancies. 59-61 It is important to note that it is not possible to detect the absence of lattice oxygen directly, but these vacancies can be inferred through the presence of adsorbed hydroxyl groups at these sites. The peak appearing at lower binding energy is attributed to lattice oxygen near oxygen-deficient sites (Figure 4B,D). The CuO_x-BM Cal. N₂ oxygen spectrum shows a similar trend to the NaBH₄-treated samples, although the peaks shifted slightly. This shift could be due to size effects or the increased covalent Cu-O bond character around a higher density of oxygen vacancies. 18

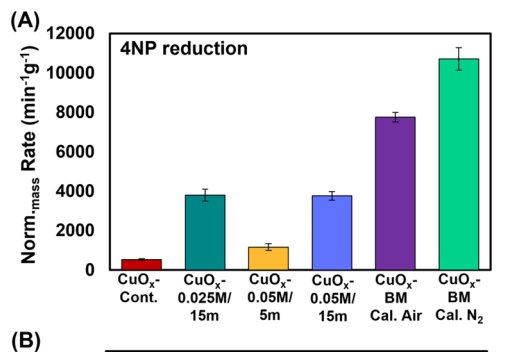
The electron paramagnetic resonance (EPR) spectrum of the $\text{CuO}_x\text{-Cont.}$ sample lacks any notable spectral features, which is consistent with the absence of vacancies in the material (Figure 5A). By contrast, the EPR spectrum of $\text{CuO}_x\text{-BM}$ Cal. N_2 (green trace) shows a broad derivative feature around $g \approx 2.02$, typical for g_\perp for S = 1/2 Cu(II) in CuO_x samples. A value for the g_\parallel resonance was not resolved due to the broadness of the signal but accounted for the asymmetry of the signal. The broadness of the signal, in part, is attributed to the unresolved hyperfine features expected for the Cu(II) centers and heterogeneity in the local environments surrounding the vacancies in the nanoparticles.

The appearance of the EPR signal in the ball-milled samples suggests an increased number of vacancies in these samples, resulting in localized paramagnetic centers. 62-65 The EPR spectrum of the CuO_x-BM Cal. Air (blue trace) sample also exhibits a similar broad S = 1/2 signal, albeit with a lower intensity than that for CuO_x-BM Cal. N₂. This result provides further evidence that the presence of O2 heals some of the vacancies during calcination. However, the CuO_x-0.05M/15m sample reveals an EPR signal similar to that of the control, even though it is confirmed to have oxygen vacancies through XPS analysis. This indicates that the vacancies producing the broad signal in the ball-milled samples likely differ from those in the NaBH₄-treated samples, corroborating that the ballmilling process may induce copper vacancies. The induction of metal vacancies in metal oxides via ball-milling is also supported by previous work.^{27,66}

Diffuse reflectance UV-vis-NIR (DR-UV-vis-NIR) spectra of the particles were used to calculate band gaps via Tauc plots (Figure 5B,C). The calculated band gap of CuO_x-Cont. was 1.29 eV; within the range of the reported band gap for bulk CuO of 1.2–1.9 eV.⁶⁷ As the CuO particles are subjected to post-treatments, their measured band gaps shift. Changes in the band gap are related to the metal oxidation state, as well as the particle size,⁶⁸ shape,⁶⁹ crystallinity,⁷⁰ microstrain,⁷¹ and oxygen vacancies.⁷² Although CuO_x-0.025M/15m incorpo-

rates some Cu₂O, which has a larger band gap range of 1.8-2.5 eV,67 the calculated band gap is slightly smaller than the control, at 1.28 eV. This is attributed to the competing impact of the increase in size and the presence of oxygen vacancies, both factors that will decrease the optical band gap. ^{68,72} As the particles are treated with higher NaBH₄ concentrations, there is a continual gradual decrease in band gap. This is not surprising as the NaBH₄ treatment is shown to propel the formation of Cu(0), which, it should be noted, impedes an accurate determination of the band gap from the Tauc plot. Furthermore, NaBH₄ treatment has been shown to increase particle size, which would lead to a further decrease in band gap. Although the CuO_x-BM Cal. Air and CuO_x-BM Cal. N₂ samples have similar size and composition to CuO_x-Cont., there are slight decreases in band gap from the control. This is attributed to the change in shape, increase in microstrain, and presence of vacancies.

Catalytic Testing and Correlations. All six nanomaterials were subjected to catalytic testing using the two probe reactions: (1) reduction of 4NP in the presence of excess NaBH₄ and (2) reduction of MB in the presence of excess NaBH₄. The observed/apparent reaction rate constants from UV—vis measurements ($k_{\rm app}$; min⁻¹) were then normalized to the mass of the catalyst used (min⁻¹ g⁻¹), a standard convention for the assessment and reporting of these reaction systems. ^{4,19} Examining the observed rates for each reaction reveals that the ball-mill-treated samples performed the best overall (Figure 6A,B). For 4NP reduction, within the CuO_x-



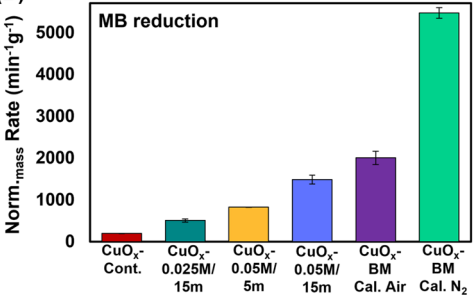


Figure 6. Observed/apparent reaction rate constants from UV–vis measurements normalized to the mass of the catalyst used (norm. $_{mass}$ rate; min^{-1} g⁻¹) for 4NP (A) and MB reduction (B).

Cont. and NaBH₄-etched samples there is no visible trend, indicating that material properties impacted by NaBH₄ treatment can be either inconsequential or competing with each other to yield no perceptible reactivity enhancement. The reduction of MB revealed more prominent trends with an increase in rate for reduction as NaBH₄ treatment increases and the ball-milled samples are the most active for this system

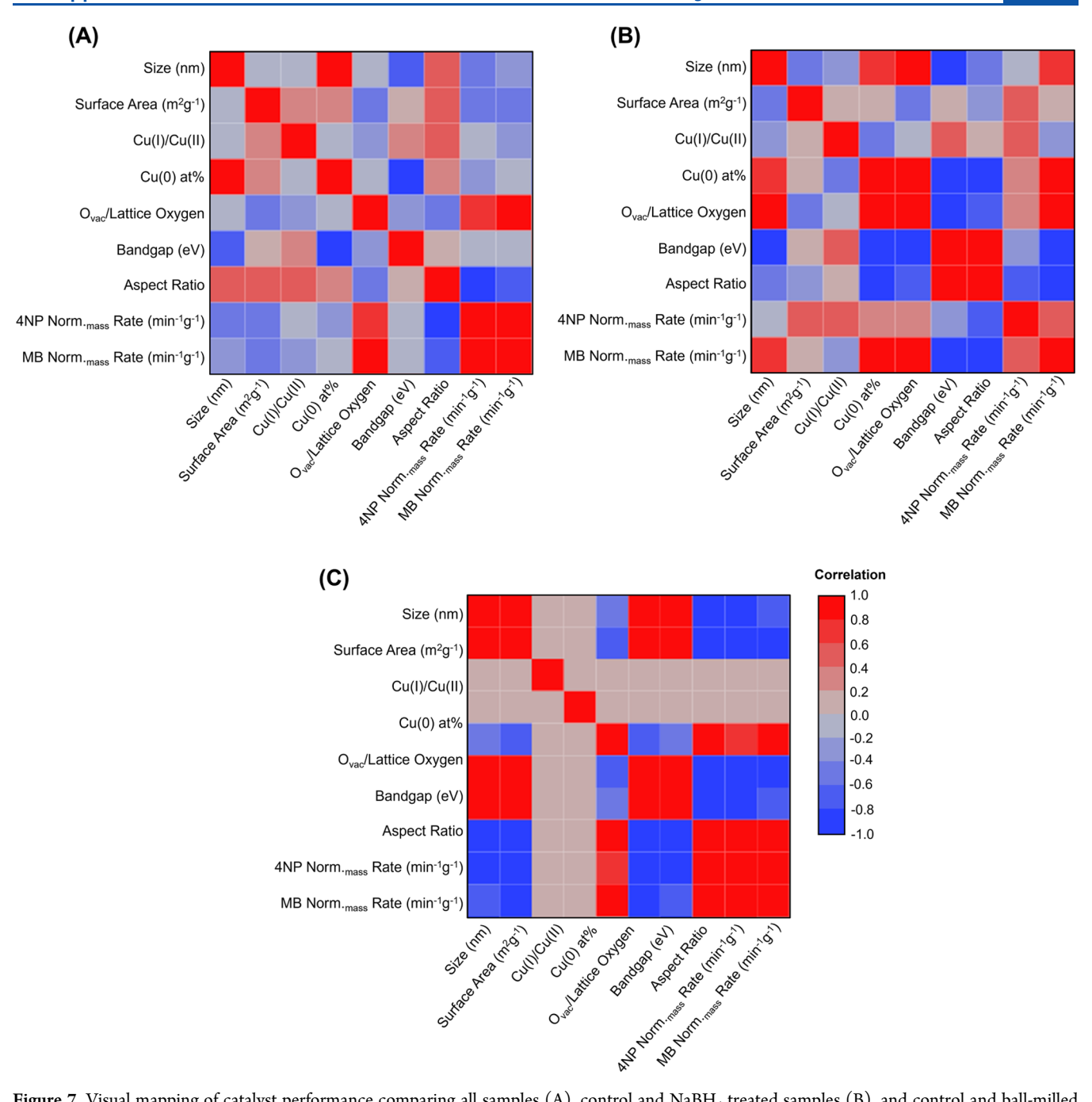


Figure 7. Visual mapping of catalyst performance comparing all samples (A), control and NaBH₄ treated samples (B), and control and ball-milled samples (C).

(Figure 6B). To disentangle the competing parameters' impact on catalytic activity, a multivariate analysis was necessary.

The multivariate analysis takes the pairwise correlation coefficient between various experimental parameters and provides a visual map of their interdependencies. The following seven independent parameters were considered: particle size, surface area, $\mathrm{Cu}(\mathrm{I})/\mathrm{Cu}(\mathrm{II})$ ratio, $\mathrm{Cu}(0)$ atom %, $O_{\mathrm{vac}}/\mathrm{lattice}$ O ratio, band gap, aspect ratio, and microstrain for pure CuO phase samples. The following two dependent parameters related to catalyst performance were considered: activities for 4NP reduction and MB reduction. Three color-coded correlation maps were produced, specifically (1) for all samples combined, (2) for the control and NaBH₄ treated

samples, and (3) for the control and ball-milled samples, as shown in Figure 7A–C, respectively.

The color scale corresponding to the value of the correlation coefficient is provided for a convenient visual representation of the parameter interdependencies. Here, red corresponds to a correlation coefficient of +1.00, while blue corresponds to a correlation coefficient of -1.00. For example, in Figure 7A, the 4NP degradation rate constant depends, to a large extent, inversely on the aspect ratio of the nanoparticles. On the other hand, the MB reduction rates show a direct dependency on the O vacancy concentration ($O_{\rm vac}$ /lattice O), i.e., increasing with the O vacancy concentration. Taken together, these color-coded correlation maps provide a convenient way to evaluate

Table 1. Catalyst Performance Correlations for Both Probe Reactions Calculated

visual map:	all data		control and NaBH ₄ -treated samples		control and BM-treated samples	
probe reaction:	4NP red.	MB red.	4NP red.	MB red.	4NP red.	MB red.
size	-0.506	-0.307	-0.049	0.662	-0.959	-0.763
surface area	-0.485	-0.573	0.579	0.196	-1.000	-0.909
Cu(I)/Cu(II)	-0.195	-0.374	0.590	-0.228	0.000	0.000
Cu(0) atom %	-0.324	-0.183	0.340	0.968	0.000	0.000
$O_{ m vac}/O_{ m lattice}$	0.647	0.892	0.279	0.803	0.724	0.941
band gap	-0.016	-0.173	-0.239	-0.927	-0.997	-0.880
aspect ratio	-0.925	-0.800	-0.637	-0.994	-0.943	-0.728
microstrain					0.990	0.962

structure-performance relationships in a multidimensional parameter space for complex catalyst systems.

Evaluating correlations within the parameters noted in Table 1, we see an inverse correlation of -0.778 between the band gap and particle size as well as an inverse correlation of -0.899between the band gap and Cu(0) atom %. These trends have been reported previously^{73,74} and, as such, serve to validate our results and analytical approach. Because the material properties were not changed linearly within a treatment protocol and particularly not between the two methods (chemical vs. milling), competing factors in the material properties prevent meaningful deconvolution for the entire data set. We speculate that it is for these reasons that we do not observe many strong correlations within the "all-data" visual map of catalyst performance (Figure 7A). However, by compartmentalizing the data based on the postmodification method (Figure 7B,C) and then reexamining the visual maps of catalyst performance, we can better disentangle these competing factors. If there is a strong correlation in both visual maps of catalyst performance, it is likely that the correlated material property does impact the corresponding catalyst performance.

First, we examine the reduction of 4NP. Between all of the visual maps of catalyst performance, we see an inverse correlation of the rate constant to nanoparticle aspect ratio (Figure 7). This is one of the strongest correlations that appears for 4NP reduction. The decrease in aspect ratio implies that there are more corner and edge sites available on the catalyst. These sites have lower coordination numbers than planar/face sites, which results in enhanced reactivity.^{33,75} Within the ball-milled samples, the microstrain additionally presents a strong correlation. The augmented microstrain leads to increased grain boundaries; these grain boundaries represent a network of edge or step sites with concomitant lower coordination, which explains the enhanced catalytic reactivity. Oxygen vacancies have previously been reported to increase the rate of 4NP reduction. We observe a correlation in our visual maps of catalyst performance to oxygen vacancies as well, but it is not as strong as that with the aspect ratio. While this indicates that oxygen vacancies play an important role in catalytic activity, they may play less of a role than corner and edge sites. Overall, the NaBH₄-treated samples' visual map of catalyst performance is the most convoluted, likely due to the competing formation of Cu(I) and subsequent phase separation with Cu₂O and metallic copper.

To further understand the impact of oxygen vacancies and reduced copper, recycling trials were undertaken using CuO_x -Cont. and CuO_x -0.05M/15m samples. Since NaBH₄ is present in the reduction reactions as the H-source and may produce oxygen vacancies and reduce the oxidation state of copper in situ, subsequent catalytic use and reuse commensu-

rate with standard catalyst recycling protocols should increase oxygen vacancies and the atomic percent of reduced copper. To test this hypothesis, five recycle trials were performed for the reduction of 4NP using CuO_x-Cont. and CuO_x-0.05M/15m to compare (Figure 8). By the second trial, both CuO_x-

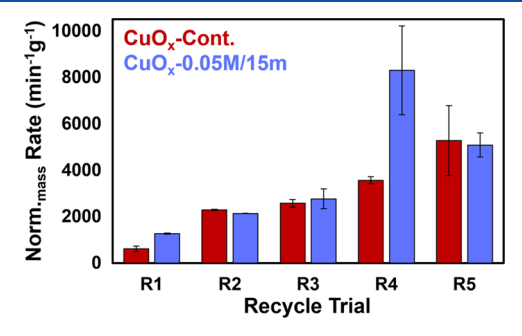


Figure 8. Recycling trials for the catalytic reduction of 4NP using $\text{CuO}_x\text{-Cont.}$ and $\text{CuO}_x\text{-0.05M}/15\text{m}$. Observed/apparent reaction rate constants from UV-vis measurements normalized to the mass of catalyst used (norm-mass rate; min $^{-1}$ g $^{-1}$).

Cont. and CuO_x-0.05M/15m showed similar catalytic activity, indicating that these catalysts likely have similar surface features (Cu oxidation state and oxygen vacancies) induced in situ. The large increase for R4 and subsequent decrease in the CuO_x-0.05M/15m series could be due to the competing benefit of oxygen vacancies being produced and agglomeration being enhanced by the presence of those vacancies. After the fifth trial, both catalysts were analyzed via XPS. No boron or nitrogen was detected in the analysis of either sample, indicating that the 4AP* and NaBH4 were desorbed from their surfaces (Figure S30). The oxygen spectra for both CuO_x -Cont. postmortem and CuO_x -0.05M/15m postmortem are nearly identical to each other, showing peaks for lattice oxygen, adsorbed hydroxyls, adsorbed molecular oxygen, and oxygen vacancies and lattice oxygen near oxygen-deficient sites (Figure S30 and Table S12). This confirms that oxygen vacancies are produced in situ during the reduction reactions with NaBH₄. Additionally, the Cu 2p HR spectra for both samples are similar to each other, revealing the presence of three peaks in both materials with similar atomic percent contributions. Specifically, peaks for Cu(II) at 11.4 \pm 0.4 atom %, Cu(I) at 37 \pm 1.3 atom %, and Cu(0) at 52 \pm 0.9 atom % were detected in both catalysts postmortem (Figure S30 and Table S13). Not only are oxygen vacancies produced during the reaction, but a triphase-metal-oxidation-state catalyst increases overall catalytic efficiency.

Critically, among the five recycle trials of both catalysts, none of the normalized rate constants reached that observed for the CuO_x -BM Cal. N_2 catalyst. It also took nearly 4 recycling trials (indicating significant exposure to excess NaBH_4) to even approximate the rate observed for CuO_x -BM Cal. Air. This corroborates that vacancies and defects produced from the ball-milling treatment are different from those chemically induced via NaBH_4 treatment. Likely, the ball-milling treatment is also inducing copper vacancies in the particles, which we postulate causes a higher microstrain that enhances catalytic reactivity (vide supra).

The reduction of MB reveals a stronger correlation to the presence of oxygen vacancies and, within the NaBH₄-treated samples, the atomic percent of Cu(0). Previously, the literature has attributed increases in MB adsorption onto the catalyst surface with an increase in the basicity of the catalyst due to enhanced attraction for cationic molecules.⁷⁶ Increased MB adsorption has also been attributed to oxygen vacancy formation, as this decreases the zeta potential of the metal oxide surface and improves electrostatic interactions.^{77,78} The adsorption is the proposed rate-limiting step,¹⁹ which explains why an increase in oxygen vacancies can improve the observed rate of MB reduction. Similar to 4NP reduction, the rate of MB reduction is also inversely correlated to the aspect ratio and directly correlated to the microstrain.

CONCLUSIONS

In summary, we were able to induce oxygen vacancies and reduce the copper metal, both partially and to total phase separation, through NaBH4 treatment to generate a series of modified CuO_x nanocatalysts. We also showed that ball-milling the parent CuO nanoparticles produces different surface defects by adding the microstrain and oxygen vacancies without reducing copper. The ball-milling likely also induces copper vacancies in the crystalline lattice; the presence of these vacancies leads to a greater enhancement in catalytic performance compared to particles subjected to NaBH₄ treatment. Testing and comparing all catalytic activities against altered material physical properties tell us that the structureactivity relationships are intrinsically linked to the specific test reaction. For 4NP reduction, the aspect ratio and microstrain were the most important, while oxygen vacancies appear to be less important than typically postulated. For MB reduction, these parameters impact the rate, but Cu(0) atom % was also important as it enhanced catalyst surface basicity, increasing MB adsorption. Importantly, this study also demonstrates secondary impacts on material properties associated with the introduction of defects via both physical and chemical means. Although the enhancement of catalytic activity is typically attributed to the presence of defects, these secondary factors can be significant. We hope that these observations will not only be useful in understanding and deconvoluting the source of enhanced reactivity in existing catalyst systems but also serve as guidelines for new nanocatalyst design.

ASSOCIATED CONTENT

Supporting Information

The Supporting Information is available free of charge at https://pubs.acs.org/doi/10.1021/acsanm.3c04897.

Experimental details, additional characterization data, and catalytic testing UV-vis spectra and kinetics (PDF)

AUTHOR INFORMATION

Corresponding Authors

Parag Banerjee — Renewable Energy and Chemical Transformations Cluster and Department of Materials Science and Engineering, University of Central Florida, Orlando, Florida 32816, United States; Florida Solar Energy Center, University of Central Florida, Cocoa, Florida 32922, United States; NanoScience and Technology Center, University of Central Florida, Orlando, Florida 32826, United States; orcid.org/0000-0003-0401-8155; Email: Parag.Banerjee@ucf.edu

Fernando J. Uribe-Romo — Department of Chemistry, University of Central Florida, Orlando, Florida 32816, United States; Renewable Energy and Chemical Transformations Cluster, University of Central Florida, Orlando, Florida 32816, United States; orcid.org/0000-0003-0212-0295; Email: Fernando@ucf.edu

Daniel R. Gamelin — Department of Chemistry, University of Washington, Seattle, Washington 98195, United States;
orcid.org/0000-0003-2888-9916; Email: Gamelin@uw.edu

Titel Jurca — Department of Chemistry, University of Central Florida, Orlando, Florida 32816, United States; Renewable Energy and Chemical Transformations Cluster, University of Central Florida, Orlando, Florida 32816, United States; NanoScience and Technology Center, University of Central Florida, Orlando, Florida 32826, United States; orcid.org/0000-0003-3656-912X; Email: Titel.Jurca@ucf.edu

Authors

Lorianne R. Shultz-Johnson — Department of Chemistry, University of Central Florida, Orlando, Florida 32816, United States; Renewable Energy and Chemical Transformations Cluster, University of Central Florida, Orlando, Florida 32816, United States

Matthew Chang — Department of Chemistry, University of Washington, Seattle, Washington 98195, United States; orcid.org/0000-0002-1409-3194

Neil N. Bisram – Department of Chemistry, University of Central Florida, Orlando, Florida 32816, United States

Jacob T. Bryant — Department of Chemistry, University of Central Florida, Orlando, Florida 32816, United States; Renewable Energy and Chemical Transformations Cluster, University of Central Florida, Orlando, Florida 32816, United States; orcid.org/0000-0002-7737-4604

Christopher P. Martin – Department of Chemistry, University of Central Florida, Orlando, Florida 32816, United States

Azina Rahmani — Department of Chemistry, University of Central Florida, Orlando, Florida 32816, United States; Renewable Energy and Chemical Transformations Cluster, University of Central Florida, Orlando, Florida 32816, United States

Jacob I. Furst — Department of Chemistry, University of Central Florida, Orlando, Florida 32816, United States; Renewable Energy and Chemical Transformations Cluster, University of Central Florida, Orlando, Florida 32816, United States; orcid.org/0009-0006-9019-2182

Jonathan D. Caranto — Department of Chemistry, University of Central Florida, Orlando, Florida 32816, United States; orcid.org/0000-0002-9196-5275

Complete contact information is available at: https://pubs.acs.org/10.1021/acsanm.3c04897

Author Contributions

The manuscript was written through contributions of all authors. All authors have given approval to the final version of the manuscript.

Funding

The authors wish to thank NSF Award #2121953 and the PREM Center for Ultrafast Dynamics and Catalysis in Emerging Materials for partially supporting this work. Work at the UW was supported in part by the National Science Foundation (NSF) through the award CHE-1904436. J.D.C. and C.P.M. were funded by NIH R35GM147515.

Notes

The authors declare no competing financial interest.

■ ACKNOWLEDGMENTS

This work was supported by the Department of Chemistry, College of Science, Department of Materials Science and Engineering, and the Faculty Cluster Initiative at the University of Central Florida. L.R.S. thanks the Ford Foundation Dissertation Fellowship and the NWRI-BioLargo Fellowship for their support. Authors acknowledge the NSF MRI: XPS: ECCS: 1726636, hosted in MCF-AMPAC facility, MSE, CECS. Part of this work was conducted at the Molecular Analysis Facility, a National Nanotechnology Coordinated Infrastructure (NNCI) site at the University of Washington, which is supported in part by funds from the National Science Foundation (awards NNCI-2025489, NNCI-1542101), the Molecular Engineering & Sciences Institute, and the Clean Energy Institute.

REFERENCES

- (1) Aditya, T.; Pal, A.; Pal, T. Nitroarene reduction: a trusted model reaction to test nanoparticle catalysts. *Chem. Commun.* **2015**, *51* (46), 9410–9431.
- (2) Belkaid, N.; Boukoussa, B.; Mokhtar, A.; Hachemaoui, M.; Beldjilali, M.; Mekki, A.; Hacini, S.; Bengueddach, A.; Hamacha, R. Antibacterial Activity and Catalytic Reduction of 4-Nitrophenol and Methylene Blue on MCM-41 Modified by CuNPs. *Silicon* **2022**, *14* (14), 8505–8516.
- (3) Begum, R.; Najeeb, J.; Sattar, A.; Naseem, K.; Irfan, A.; Al-Sehemi, A. G.; Farooqi, Z. H. Chemical reduction of methylene blue in the presence of nanocatalysts: a critical review. *Rev. Chem. Eng.* **2020**, *36* (6), 749–770.
- (4) Shultz, L. R.; Hu, L.; Preradovic, K.; Beazley, M. J.; Feng, X.; Jurca, T. A broader-scope analysis of the catalytic reduction of nitrophenols and azo dyes with noble metal nanoparticles. *ChemCatChem* **2019**, *11* (11), 2590–2595.
- (5) Wang, D.; Astruc, D. The recent development of efficient Earthabundant transition-metal nanocatalysts. *Chem. Soc. Rev.* **2017**, *46* (3), 816–854.
- (6) Formenti, D.; Ferretti, F.; Scharnagl, F. K.; Beller, M. Reduction of nitro compounds using 3d-non-noble metal catalysts. *Chem. Rev.* **2019**, *119* (4), 2611–2680.
- (7) Wang, W.; Deng, C.; Xie, S.; Li, Y.; Zhang, W.; Sheng, H.; Chen, C.; Zhao, J. Photocatalytic C-C coupling from carbon dioxide reduction on copper oxide with mixed-valence copper (I)/copper (II). J. Am. Chem. Soc. 2021, 143 (7), 2984–2993.
- (8) Chen, Y.; Wang, M.; Ma, Y.; Li, Y.; Cai, J.; Li, Z. Coupling photocatalytic CO₂ reduction with benzyl alcohol oxidation to produce benzyl acetate over Cu₂O/Cu. *Catal. Sci. Technol.* **2018**, 8 (8), 2218–2223.
- (9) Bisht, N. S.; Mehta, S.; Sahoo, N. G.; Dandapat, A. The room temperature synthesis of a CuO-Bi-BiOBr ternary Z-scheme photocatalyst for enhanced sunlight driven alcohol oxidation. *Dalton Trans.* **2021**, *50* (14), 5001–5010.

- (10) Gusain, R.; Kumar, P.; Sharma, O. P.; Jain, S. L.; Khatri, O. P. Reduced graphene oxide—CuO nanocomposites for photocatalytic conversion of CO₂ into methanol under visible light irradiation. *Appl. Catal., B* **2016**, *181*, 352–362.
- (11) Sasmal, A. K.; Dutta, S.; Pal, T. A ternary Cu₂O-Cu-CuO nanocomposite: a catalyst with intriguing activity. *Dalton Trans.* **2016**, 45 (7), 3139–3150.
- (12) Filiz, B. C. The role of catalyst support on activity of copper oxide nanoparticles for reduction of 4-nitrophenol. *Adv. Powder Technol.* **2020**, 31 (9), 3845–3859.
- (13) Sarkar, C.; Dolui, S. K. Synthesis of copper oxide/reduced graphene oxide nanocomposite and its enhanced catalytic activity towards reduction of 4-nitrophenol. *RSC Adv.* **2015**, *5* (75), 60763–60769
- (14) Yu, Y.; Guo, H.; Wang, P.; Zhai, S.; Han, J.; Li, W.; Wang, Y.; Wang, Y. Catalytic reduction of 4-nitrophenol using Cu/Cu₂O nanocomposites based on magnetic maize straw. *Res. Chem. Intermed.* **2023**, 49 (2), 381–397.
- (15) Boon, A. Q.; van Looij, F.; Geus, J. W. Influence of surface oxygen vacancies on the catalytic activity of copper oxide: Part 1. Oxidation of carbon monoxide. *J. Mol. Catal.* **1992**, *75* (3), 277–291.
- (16) Wang, Y.; Yun, J.; Zhu, L.; Cao, B.; Gao, J.; Shi, X.; Huang, Y.; Liu, P.; Zhu, G. Mechanistic study of low-temperature CO oxidation over CuO/Cu₂O interfaces with oxygen vacancy modification. *Appl. Surf. Sci.* **2022**, *603*, No. 154469.
- (17) Shaw, M.; Samanta, D.; Bera, S.; Mahto, M. K.; Shaik, M. A. S.; Konar, S.; Mondal, I.; Dhara, D.; Pathak, A. Role of Surface Oxygen Vacancies and Oxygen Species on CuO Nanostructured Surfaces in Model Catalytic Oxidation and Reductions: Insight into the Structure—Activity Relationship Toward the Performance. *Inorg. Chem.* **2022**, *61* (37), 14568—14581.
- (18) Zhang, J.; Wang, Z.; Chen, W.; Xiong, Y.; Cheong, W.-C.; Zheng, L.; Yan, W.; Gu, L.; Chen, C.; Peng, Q.; Hu, P.; Wang, D.; Li, Y. Tuning Polarity of Cu-O Bond in Heterogeneous Cu Catalyst to Promote Additive-free Hydroboration of Alkynes. *Chem* **2020**, *6* (3), 725–737.
- (19) Shultz, L. R.; Preradovic, K.; Ghimire, S.; Hadley, H. M.; Xie, S.; Kashyap, V.; Beazley, M. J.; Crawford, K. E.; Liu, F.; Mukhopadhyay, K.; Jurca, T. Nickel foam supported porous copper oxide catalysts with noble metal-like activity for aqueous phase reactions. *Catal. Sci. Technol.* **2022**, *12* (12), 3804–3816.
- (20) Wang, Z.; Lin, R.; Huo, Y.; Li, H.; Wang, L. Formation, detection, and function of oxygen vacancy in metal oxides for solar energy conversion. *Adv. Funct. Mater.* **2022**, *32* (7), No. 2109503.
- (21) Ji, Q.; Bi, L.; Zhang, J.; Cao, H.; Zhao, X. S. The role of oxygen vacancies of ABO₃ perovskite oxides in the oxygen reduction reaction. *Energy Environ. Sci.* **2020**, *13* (5), 1408–1428.
- (22) He, J.; Wu, P.; Lu, L.; Li, H.; Ji, H.; He, M.; Jia, Q.; Hua, M.; Zhu, W.; Li, H. Lattice-Refined Transition-Metal Oxides via Ball Milling for Boosted Catalytic Oxidation Performance. ACS Appl. Mater. Interfaces 2019, 11 (40), 36666–36675.
- (23) Najafi, M.; Azizian, S. Catalytic reduction of 4-nitrophenol on the surface of copper/copper oxide nanoparticles: a kinetics study. *Appl. Nanosci.* **2020**, *10* (10), 3827–3837.
- (24) Wang, Y.; Tao, S.; Lin, H.; Han, S.; Zhong, W.; Xie, Y.; Hu, J.; Yang, S. NaBH4 induces a high ratio of Ni³⁺/Ni²⁺ boosting OER activity of the NiFe LDH electrocatalyst. *RSC Adv.* **2020**, *10* (55), 33475–33482.
- (25) Zhuang, G.; Chen, Y.; Zhuang, Z.; Yu, Y.; Yu, J. Oxygen vacancies in metal oxides: recent progress towards advanced catalyst design. *Sci. China Mater* **2020**, *63* (11), 2089–2118.
- (26) Yang, Y.; Zhang, S.; Wang, S.; Zhang, K.; Wang, H.; Huang, J.; Deng, S.; Wang, B.; Wang, Y.; Yu, G. Ball milling synthesized MnOx as highly active catalyst for gaseous POPs removal: significance of mechanochemically induced oxygen vacancies. *Environ. Sci. Technol.* **2015**, 49 (7), 4473–4480.
- (27) Kavitha, M. K.; Jinesh, K.; Philip, R.; Gopinath, P.; John, H. Defect engineering in ZnO nanocones for visible photoconductivity

- and nonlinear absorption. Phys. Chem. Chem. Phys. 2014, 16 (45), 25093-25100.
- (28) Zhang, X.; Tang, P.; Zhai, G.; Lin, X.; Zhang, Q.; Chen, J.; Wei, X. Regulating phase junction and oxygen vacancies of TiO_2 nanoarrays for boosted photoelectrochemical water oxidation. *Chem. Res. Chin. Univ.* **2022**, 38 (5), 1292–1300.
- (29) Martín-Gómez, J.; Hidalgo-Carrillo, J.; Montes, V.; Estevez-Toledano, R. C.; Escamilla, J. C.; Marinas, A.; Urbano, F. J. EPR and CV studies cast further light on the origin of the enhanced hydrogen production through glycerol photoreforming on CuO:TiO₂ physical mixtures. *J. Environ. Chem. Eng.* **2021**, *9* (4), No. 105336.
- (30) Viano, A.; Mishra, S.; Lloyd, R.; Losby, J.; Gheyi, T. Thermal effects on ESR signal evolution in nano and bulk CuO powder. *J. Non-Cryst. Solids* **2003**, 325 (1–3), 16–21.
- (31) Ndala, Z. B.; Nkabinde, S. S.; Shumbula, N. P.; Makgae, O. A.; Kolokoto, T.; Ek, M.; Gqoba, S. S.; Linganiso, C. E.; Mdluli, P. S.; Moloto, N. Unraveling the effects of surface functionalization on the catalytic activity of ReSe₂ nanostructures towards the hydrogen evolution reaction. *Appl. Surf. Sci.* **2023**, *612*, No. 155971.
- (32) Puigdollers, A. R.; Schlexer, P.; Tosoni, S.; Pacchioni, G. Increasing Oxide Reducibility: The Role of Metal/Oxide Interfaces in the Formation of Oxygen Vacancies. *ACS Catal.* **2017**, *7* (10), 6493–6513.
- (33) Ni, B.; Wang, X. Face the edges: catalytic active sites of nanomaterials. *Adv. Sci.* **2015**, 2 (7), No. 1500085.
- (34) Ponce, A. A.; Klabunde, K. J. Chemical and catalytic activity of copper nanoparticles prepared via metal vapor synthesis. *J. Mol. Catal. A: Chem.* **2005**, 225 (1), 1–6.
- (35) Teo, J. J.; Chang, Y.; Zeng, H. C. Fabrications of hollow nanocubes of Cu₂O and Cu via reductive self-assembly of CuO nanocrystals. *Langmuir* **2006**, 22 (17), 7369–7377.
- (36) Qin, Y.; Zhang, F.; Chen, Y.; Zhou, Y.; Li, J.; Zhu, A.; Luo, Y.; Tian, Y.; Yang, J. Hierarchically porous CuO hollow spheres fabricated via a one-pot template-free method for high-performance gas sensors. *J. Phys. Chem. C* **2012**, *116* (22), 11994–12000.
- (37) Kassem, A. A.; Abdelhamid, H. N.; Fouad, D. M.; Ibrahim, S. A. Hydrogenation reduction of dyes using metal-organic framework-derived CuO@C. *Microporous Mesoporous Mater.* **2020**, 305, No. 110340.
- (38) Peng, M. M.; Hemalatha, P.; Ganesh, M.; Vinodh, R.; Jang, H. T. Synthesis and Characterization of Novel Mesoporous CuO and Its Application to CO₂ Capture. *Asian J. Chem.* **2013**, *25* (17), No. 9941.
- (39) Massarotti, V.; Capsoni, D.; Bini, M.; et al. X-ray powder diffraction ab initio structure solution of materials from solid state synthesis: the copper oxide case. *Z. Kristallogr. Cryst. Mater.* **1998**, 213 (5), 259–265.
- (40) Wang, W.; Liao, Z.; Wang, Y.; Wu, X.; Qu, F.; Zhang, X. Hydrothermal synthesis of highly symmetric 26-facet Cu₂O polyhedra. *Cryst. Res. Technol.* **2011**, *46* (3), 300–304.
- (41) Rao, S. S.; Anantharaman, T. Accurate evaluation of lattice parameters of α -brasses. *Curr. Sci.* **1963**, 32 (6), 262–263.
- (42) Toby, B. H.; Von Dreele, R. B. GSAS-II: the genesis of a modern open-source all purpose crystallography software package. *J. Appl. Crystallogr.* **2013**, *46* (2), 544–549.
- (43) Daly, R.; Khitouni, M.; Kolsi, A. W.; Njah, N. The studies of crystallite size and microstrains in aluminum powder prepared by mechanical milling. *Phys. Status Solidi C* **2006**, *3* (9), 3325–3331.
- (44) Khayati, G.; Nourafkan, E.; Karimi, G.; Moradgholi, J. Synthesis of cuprous oxide nanoparticles by mechanochemical oxidation of copper in high planetary energy ball mill. *Adv. Powder Technol.* **2013**, 24 (1), 301–305.
- (45) Goldstein, H. F.; Kim, D.-s.; Peter, Y. Y.; Bourne, L.; Chaminade, J.; Nganga, L. Raman study of CuO single crystals. *Phys. Rev. B* **1990**, 41 (10), No. 7192.
- (46) Chrzanowski, J.; Irwin, J. Raman scattering from cupric oxide. *Solid State Commun.* **1989**, 70 (1), 11–14.
- (47) Xu, J.; Ji, W.; Shen, Z.; Li, W.; Tang, S.; Ye, X.; Jia, D.; Xin, X. Raman spectra of CuO nanocrystals. *J. Raman Spectrosc.* **1999**, 30 (5), 413–415.

- (48) Davó-Quiñonero, A.; Bailon-Garcia, E.; Lopez-Rodriguez, S.; Juan-Juan, J.; Lozano-Castello, D.; García-Melchor, M.; Herrera, F. C.; Pellegrin, E.; Escudero, C.; Bueno-Lopez, A. Insights into the oxygen vacancy filling mechanism in CuO/CeO₂ catalysts: a key step toward high selectivity in preferential CO oxidation. *ACS Catal.* **2020**, *10* (11), 6532–6545.
- (49) Said, M. I.; Othman, A.; Abd elhakeem, E. M. Structural, optical and photocatalytic properties of mesoporous CuO nanoparticles with tunable size and different morphologies. *RSC Adv.* **2021**, *11* (60), 37801–37813.
- (50) Devamani, R. H. P.; Alagar, M. Synthesis and characterisation of copper II hydroxide nano particles. *Nano Biomed. Eng.* **2013**, *5* (3), 116–120.
- (51) Rao, M. P.; Wu, J. J.; Asiri, A. M.; Anandan, S.; Ashokkumar, M. Photocatalytic properties of hierarchical CuO nanosheets synthesized by a solution phase method. *J. Environ. Sci.* **2018**, *69*, 115–124.
- (52) Tahir, D.; Tougaard, S. Electronic and optical properties of Cu, CuO and Cu_2O studied by electron spectroscopy. *J. Phys.: Condens. Matter* **2012**, 24 (17), No. 175002.
- (53) Stadnichenko, A. I.; Sorokin, A.; Boronin, A. XPS, UPS, and STM studies of nanostructured CuO films. *J. Struct. Chem.* **2008**, *49*, 341–347.
- (54) Pauly, N.; Tougaard, S.; Yubero, F. Determination of the Cu 2p primary excitation spectra for Cu, Cu₂O and CuO. *Surf. Sci.* **2014**, 620, 17–22.
- (55) Miller, A. C.; Simmons, G. W. Copper by XPS. Surf. Sci. Spectra **1993**, 2 (1), 55–60.
- (56) Vasquez, R. P. Cu₂O by XPS. Surf. Sci. Spectra 1998, 5 (4), 257-261.
- (57) Dan, Z.; Yang, Y.; Qin, F.; Wang, H.; Chang, H. Facile fabrication of Cu₂O nanobelts in ethanol on nanoporous Cu and their photodegradation of methyl orange. *Materials* **2018**, *11* (3), No. 446.
- (58) Ethiraj, A. S.; Kang, D. J. Synthesis and characterization of CuO nanowires by a simple wet chemical method. *Nanoscale Res. Lett.* **2012**, *7* (1), No. 70.
- (59) Wang, Y.; Lü, Y.; Zhan, W.; Xie, Z.; Kuang, Q.; Zheng, L. Synthesis of porous Cu₂O/CuO cages using Cu-based metal—organic frameworks as templates and their gas-sensing properties. *J. Mater. Chem. A* **2015**, 3 (24), 12796–12803.
- (60) Zheng, X.; Li, P.; Zheng, S.; Zhang, Y. Thermal decomposition of ammonium perchlorate in the presence of Cu(OH)₂· 2Cr(OH)₃ nanoparticles. *Powder Technol.* **2014**, *268*, 446−451.
- (61) Idriss, H. On the wrong assignment of the XPS O1s signal at 531–532 eV attributed to oxygen vacancies in photo-and electrocatalysts for water splitting and other materials applications. *Surf. Sci.* **2021**, 712, No. 121894.
- (62) Yang, X.; Lai, C.; Li, L.; Cheng, M.; Liu, S.; Yi, H.; Zhang, M.; Fu, Y.; Xu, F.; Yan, H.; et al. Oxygen vacancy assisted Mn-CuO Fenton-like oxidation of ciprofloxacin: performance, effects of pH and mechanism. *Sep. Purif. Technol.* **2022**, 287, No. 120517.
- (63) Zhang, K.; Yang, L.; Hu, Y.; Fan, C.; Zhao, Y.; Bai, L.; Li, Y.; Shi, F.; Liu, J.; Xie, W. Synthesis of a Gold–Metal Oxide Core—Satellite Nanostructure for In Situ SERS Study of CuO-Catalyzed Photooxidation. *Angew. Chem.* **2020**, *132* (41), 18159–18165.
- (64) Martinez-Arias, A.; Fernández-Garcia, M.; Gálvez, O.; Coronado, J.; Anderson, J.; Conesa, J. C.; Soria, J.; Munuera, G. Comparative study on redox properties and catalytic behavior for CO oxidation of CuO/CeO₂ and CuO/ZrCeO4 catalysts. *J. Catal.* **2000**, 195 (1), 207–216.
- (65) Azzoni, C. B.; Paleari, A.; Parravicini, G. On the low-temperature magnetic properties of CuO single crystals. *J. Phys.: Condens. Matter* **1992**, 4 (5), No. 1359.
- (66) Li, J.; Liu, Z.; Ma, W.; Dong, H.; Zhang, K.; Wang, R. Low-temperature synthesis of cubic phase Li₇La₃Zr₂O₁₂ via sol-gel and ball milling induced phase transition. *J. Power Sources* **2019**, *412*, 189–196.
- (67) Oudah, M.; Hasan, M.; Abd, A. In Synthesis of Copper Oxide Thin Films by Electrolysis Method Based on Porous Silicon for Solar Cell

- Applications, IOP Conference Series: Materials Science and Engineering; IOP Publishing, 2020; p 012051.
- (68) Jeyarani, W. J.; Tenkyong, T.; Bachan, N.; Kumar, D. A.; Shyla, J. M. An investigation on the tuning effect of glucose-capping on the size and bandgap of CuO nanoparticles. *Adv. Powder Technol.* **2016**, 27 (2), 338–346.
- (69) Singh, M.; Singhal, A. In Modeling of Shape and Size Effects for the Band Gap of Semiconductor Nanoparticles, 2nd International Conference on Micro-Electronics and Telecommunication Engineering (ICMETE); IEEE, 2018; pp 339—342.
- (70) Zhang, F.; Li, H.; Cui, Y.-T.; Li, G.-L.; Guo, Q. Evolution of optical properties and band structure from amorphous to crystalline Ga₂O₃ films. *AIP Adv.* **2018**, 8 (4), No. 045112.
- (71) Udayabhaskar, R.; Karthikeyan, B. Role of micro-strain and defects on band-gap, fluorescence in near white light emitting Sr doped ZnO nanorods. *J. Appl. Phys.* **2014**, *116* (9), No. 094310.
- (72) Liu, H.; Zeng, F.; Lin, Y.; Wang, G.; Pan, F. Correlation of oxygen vacancy variations to band gap changes in epitaxial ZnO thin films. *Appl. Phys. Lett.* **2013**, *102* (18), No. 181908.
- (73) Singh, M.; Goyal, M.; Devlal, K. Size and shape effects on the band gap of semiconductor compound nanomaterials. *J. Taibah Univ. Sci.* **2018**, *12* (4), 470–475.
- (74) Munir, S.; Shah, S. M.; Hussain, H.; khan, R. A. Effect of carrier concentration on the optical band gap of TiO_2 nanoparticles. *Mater. Des.* **2016**, 92, 64–72.
- (75) Jin, L.; Liu, B.; Duay, S. S.; He, J. Engineering Surface Ligands of Noble Metal Nanocatalysts in Tuning the Product Selectivity. *Catalysts* **2017**, *7* (2), No. 44.
- (76) Iqbal, K.; Iqbal, A.; Kirillov, A. M.; Liu, W.; Tang, Y. Hybrid metal—organic-framework/inorganic nanocatalyst toward highly efficient discoloration of organic dyes in aqueous medium. *Inorg. Chem.* **2018**, *57* (21), 13270–13278.
- (77) Ranjbari, A.; Kim, J.; Kim, J. H.; Yu, J.; Demeestere, K.; Heynderickx, P. M. Enhancement of commercial ZnO adsorption and photocatalytic degradation capacity of methylene blue by oxygen vacancy modification: Kinetic study. *Catal. Today* **2023**, *413*–*415*, No. 113976.
- (78) Ren, P.; Ren, X.; Xu, J.; Li, H.; Zheng, Y.; Hong, Y.; Lin, Y.; Zhou, Y.; Chen, Y.; Zhang, W. Excellent adsorption property and mechanism of oxygen vacancies-assisted hexagonal MoO₃ nanosheets for methylene blue and rhodamine b dyes. *Appl. Surf. Sci.* **2022**, 597, No. 153699.